

U.S. DEPARTMENT OF COMMERCE  
National Technical Information Service

AD-A027 713

THEORY AND CALCULATION FOR THE DISPLACEMENTS  
AND STRESSES AT AN EARTHQUAKE SOURCE

LAMONT-DOHERTY GEOLOGICAL OBSERVATORY

PREPARED FOR  
AIR FORCE OFFICE OF SCIENTIFIC RESEARCH

1 JUNE 1976

OSR - TR - 76 - 2338

219117

ADA 027713

AFOSR-D44129-74-C-0029

THEORY AND CALCULATION FOR THE DISPLACEMENTS AND STRESSES AT AN EARTHQUAKE SOURCE

Paul G. Richards

Columbia University  
Lamont-Doherty Geological Observatory  
Palisades, New York 10964

1 June 1976

Final Report  
1 October 1973 - 31 March 1976

Approved for public release; distribution unlimited

Sponsored by Advanced Research Projects Agency  
ARPA Order No. 1827-11

AIR FORCE OFFICE OF SCIENTIFIC RESEARCH  
1400 Wilson Boulevard  
Arlington, Virginia 22209

D D C  
RECEIVED  
AUG 3 1976  
RESERVED  
A

AIR FORCE OFFICE OF SCIENTIFIC RESEARCH (AFOSR)  
NOTICE OF TRANSMITTAL TO THE  
This technical report has been reviewed and is  
approved for public release (AS AR 180-12 (76)).  
Distribution is unlimited.  
A. D. BLISS  
Technical Information Officer

REPRODUCED BY  
NATIONAL TECHNICAL  
INFORMATION SERVICE  
U. S. DEPARTMENT OF COMMERCE  
SPRINGFIELD, VA 22161

# DISCLAIMER NOTICE

THIS DOCUMENT IS THE BEST  
QUALITY AVAILABLE.

COPY FURNISHED CONTAINED  
A SIGNIFICANT NUMBER OF  
PAGES WHICH DO NOT  
REPRODUCE LEGIBLY.

Table of Contents

	<u>Page</u>
(1) First Strong Motion Records from a Central or Eastern United States Earthquake	1
(2) Source Properties of a Blue Mountain Lake Earthquake	1
(3) Comparison of Strong Ground Motion from Several Dislocation Models	2
(4) The Dynamic Field of a Growing Plane Elliptical Shear Crack	3
(5) Motions Near a Shallow Rupturing Fault: Evaluation of Effects due to the Free Surface	4
(6) List of Publications	4
(7) Appendix	5

D D C  
RECEIVED  
AUG 3 1976  
RECEIVED  
A

A

(1) First Strong Motion Records from a Central or Eastern United States Earthquake. (Fletcher and Anderson)

Two strong motion accelerographs were installed at Blue Mountain Lake, New York (BML) shortly after the initiation of a swarm-type sequence of earthquakes in mid-July of 1973. Three records rich in frequencies as high as 35 Hz were obtained from two of the largest events (magnitude 2.7 and 2.6), the foci of which are between 1.0 and 4 km from the accelerograph stations. The maximum acceleration recorded was  $+0.034$  g at 25 Hz. These are the first strong-motion records obtained from east of the Rocky Mountains. Since strong-motion results from the western United States may not be applicable to the eastern two-thirds of the U.S., these new results have important implications for the design of critical facilities such as nuclear power plants, liquified gas storage tanks, and large dams.

A paper on this material has been published (see page 4).

(2) Source Properties of a Blue Mountain Lake Earthquake.  
(Anderson and Fletcher)

An accelerogram obtained at Blue Mt. Lake, New York is remarkable for the simplicity of its S-wave pulse. This results from 1) a nearly complete absence of scattering and reflections as second arrivals on the accelerogram and 2) a very elementary earthquake source. The earth-

quake identified with this accelerogram had a magnitude  $m_b = 2.2$  and a hypocentral distance of about 1 km from the accelerometer. Spectral analysis of the S-wave indicates the earthquake had a moment of  $8 \times 10^{18}$  dyne-cm, and a source radius of 20 to 40 m. When the accelerogram is integrated to obtain displacement, there is a step offset of about 5 microns associated with a near field component of the S-wave pulse. The S-wave, including the step offset, can be matched in remarkable detail by a dislocation model with a moment of  $8.4 \times 10^{18}$  dyne-cm.

A paper on this material has been published (see page 4).

(3) Comparison of Strong Ground Motion from Several Dislocation Models. (Anderson and Richards)

To examine the effects of different earthquake sources, ground motion near the rupture for several dislocation models has been calculated. Quite different dislocation models of the rupture can give very similar displacements at stations located only one fault dimension from the fault in an infinite homogeneous elastic space. In particular: 1) models with fault motions and rupture geometry quite different from Haskell's propagating ramp can often have near-field motions very similar to those from a ramp model; and 2) quite similar near-field motions are found, for different ramp models in which the rupture velocity and

rise time are varied together over rather large ranges (e.g., a factor of three in rise time).

We infer that there is considerable ambiguity in interpreting near-field displacement data in terms of a model of fault motion. The ambiguity may be reduced by using acceleration data, although this entails a considerable increase in computer time for solving forward problems.

A paper on this material has been published (see page 4).

(4) The Dynamic Field of a Growing Plane Elliptical Shear Crack. (Richards)

The radiation for a three-dimensional problem of brittle fracture is investigated. A crack is presumed to nucleate at a point in an infinite pre-stressed elastic medium, and the crack subsequently grows steadily with subsonic rupture velocities, maintaining the shape of an ellipse. Shear stresses are relieved by the crack, and exact solutions are derived for the acceleration and stress-rate (at every point of the medium) in terms of single integrals and algebraic expressions. The solutions are evaluated analytically at wavefronts and singularities, and numerically, at different points in the medium, for different growth rates of the crack.

A paper on this material has been published (see page 4).

(5) Motions Near a Shallow Rupturing Fault: Evaluation of Effects due to the Free Surface. (Anderson)

A full-size report on this topic is attached herewith as an appendix. Report consists of 22 text pages, 5 appendix pages, 2 reference pages, 17 figure caption and figure pages, and 1 table.

This material has been accepted for publication (see page 4).

(6) List of Publications

First Strong Motion Records from a Central or Eastern United States Earthquake by J. B. Fletcher and J. Anderson. Bull. Seismol. Soc. Amer., 64, 1455-1466, 1974.

Source Properties of a Blue Mountain Lake Earthquake by J. Anderson and J. Fletcher, in press, Bull. Seismol. Soc. Amer., August 1976.

Comparison of Strong Ground Motion from Several Dislocation Models by J. Anderson and P. G. Richards. Geophys. J. Roy. astr. Soc., 42, 347-373, 1975.

The Dynamic Field of a Growing Plane Elliptical Shear Crack by P. G. Richards. Int. J. Solids Structures, 9, 843-861, 1973.

Motions Near a Shallow Rupturing Fault: Evaluation of Effects due to the Free Surface by J. G. Anderson, in press, Geophys. J. Roy. astr. Soc., 1976

- (7) APPENDIX: Motions Near a Shallow Rupturing Fault:  
Evaluation of Effects due to the Free Surface.  
(Anderson)

MOTIONS NEAR A SHALLOW RUPTURING FAULT:  
EVALUATION OF EFFECTS DUE TO THE FREE SURFACE\*

John G. Anderson

Lamont-Doherty Geological Observatory

of Columbia University

Palisades, New York 10964

and

Department of Geological Sciences

Columbia University

ABSTRACT

The displacement of the surface of a half space near a shallow rupturing fault is, generally, approximated poorly by the method of doubling the amplitude calculated for the same source in an infinite space. To obtain this result, the motions of a half space were calculated using a Green's function which is a solution to Lamb's problem, and the motions of an infinite space were calculated using the formulae of Haskell. The infinite space method does work well for two cases: 1. A fault from which the angles of incidence at the station are less than 30 degrees and 2. Horizontal components of motion dominated by SH waves (as from a strike slip fault) with angles of incidence less than 80 degrees.

---

\*Lamont-Doherty Geological Observatory Contribution No. 0000.

Reproduced from  
best available copy.

## INTRODUCTION

The surface motions resulting from a point source in a half space include four major effects which are absent in an infinite space: The amplification of all waves; the phase shift of SV-waves incident at angles greater than critical; the SP-phase, which travels to the surface as an SV-wave at the critical angle and is then refracted horizontally as a P-wave; and Rayleigh waves. These effects have all been studied before from a point source (e.g. Anopoff *et al.*, 1957; Pekeris and Lifson, 1957; Kawasaki *et al.*, 1973), the present objective is to evaluate the effect of including the free surface when the source is a spatially extended rupture. This allows a critical evaluation of the assumption, used frequently in dislocation modeling, that the free surface may be reasonably accounted for by doubling the amplitude of motions in an infinite space (e.g. Kanamori, 1972; Trifunac, 1974; Trifunac and Udawadia, 1974; Anderson, 1974).

## METHOD

The displacements of the surface of a half space are calculated by applying the representation theorem (Burridge and Knopoff, 1964):

$$U_i(\bar{x}, t) = \int_{-\infty}^{\infty} dt' \iint_S \mu n_k(\bar{\xi}) [u_j(\bar{\xi}, t')] \left( \varepsilon_{ij,k'}(\bar{x}, t-t'; \bar{\xi}, 0) + \varepsilon_{ik,j'}(\bar{x}, t-t'; \bar{\xi}, 0) \right) d\xi_1 d\xi_2. \quad (1)$$

Here  $U_i$  is the  $i$ th component of displacement of the surface,  $\mu$  the shear modulus,  $n_k$  the  $k$ th component of the normal to the fault, and  $[u_j]$  the amplitude of the dislocation on the fault. The integration is over time and the fault surfaces. The Green's function is

$\varepsilon_{ij,k'} = \frac{d}{d\xi_k} \varepsilon_{ij}$ , where  $\varepsilon_{ij}$  is the displacement in the  $i$  direction at location  $\bar{x}$ , time  $t$  due to an impulse force in the  $j$  direction at location  $\bar{\xi}$ , time  $t'$ . Thus,  $\varepsilon_{ij,k'}$  is the displacement due to a point couple, and the sum  $(\varepsilon_{ij,k'} + \varepsilon_{ik,j'})$  is the displacement due to a double couple force, or, equivalently, due to a point dislocation. It is of the form

$$\varepsilon_{ij,k'} = \frac{d^2}{dt^2} h_{ij,k'}$$

where  $h_{ij,k'}$  is evaluated by an integral in the complex plane given by Johnson (1974). The differentiation must be done numerically. As a function of time  $t_0 = t-t'$ ,  $h_{ij,k'}$  is a Green's function for a force which is zero for  $t_0 < 0$  and has magnitude  $t_0$  for  $t_0 > 0$ .

This series of integrations and differentiations was handled as follows:

- Step 1. The Green's functions are computed (using a Romberg integration subroutine) and stored for an array of points on the fault. The differentiation with respect to time is deferred until the second step. These are computed only once for each fault-station geometry.
- Step 2. The source time function for each grid point is convolved with the corresponding Green's function to perform the time integral. The results from all the points on the fault plane are weighted and summed to perform the spatial integration. The weight of a grid point is the area of the fault inside a rectangle, centered on the grid point, with sides equal to the grid spacing. Thus, the sum of the weights is equal to the fault area. The sum of the convolved functions is differentiated numerically to obtain the desired displacement at the station.

Because the spatial limits of integration are a function of time, it is necessary to justify taking the time differentiation outside the spatial integral. This is allowable because the integration is approximated numerically by a sum, where the weight of the Green's function for each grid point is independent of time. The errors due to this approximation are discussed below. Because the weights are constants, it does not matter whether the sum or the numerical differentiation is done first.

In finding a dislocation model for an earthquake, the fault-station geometry is known, and displacements at the station are typically calculated for several trial models of rupture. The two step method is excellent in this situation, because storing the Green's functions as in step 1 is more economical than recomputing them.

The displacements from a dislocation in an infinite space are calculated as described in Anderson and Richards (1975). The coordinate system for all models is shown in Figure 1. The P-wave velocity  $\alpha = 6.0$  km/sec and the S-wave velocity  $\beta = 3.4$  km/sec was used throughout.

A propagating ramp dislocation time function is used here, but any other time function could have been used.

In this model,

$$\left[ u(\xi_1, \xi_3, t) \right] = \begin{cases} 0 & |\xi_1| > \frac{L_1}{2} \text{ or } |\xi_3| > \frac{L_3}{2} \\ 0 & t - \frac{\xi_1}{v} \leq 0 \\ \frac{D_m}{\tau} \left( \frac{t - \xi_1}{v} \right) & 0 < t - \frac{\xi_1}{v} < \tau \\ D_m & \tau \leq t - \frac{\xi_1}{v} \end{cases}$$

where  $L_1, L_3$  are the fault dimensions,  $v$  is the rupture velocity,  $\tau$  is the rise time, and  $D_m$  is the final displacement on the fault.

Four integrals must be approximated by sums to compute displacement at a station on a half space. These approximations are sources of errors in the final waveform because only a finite number of sums can be done on a computer. Approximating the three integrations shown explicitly in eq. (1) gives rise to an upper limit ( $f_g$ , say) to the frequencies which are meaningfully represented in the computed displacements. A method of evaluating  $f_g$  is presented next. Then the effect of errors from approximating the integration to obtain the Green's function is considered.

To estimate  $f_g$ , consider a source with an impulse time function traveling with velocity  $v$  along a short line of length  $L$ . The radiation at a distant station is a square wave, with duration  $T_0$  and amplitude 1, say. The Fourier amplitude spectrum is

$$F_e(\omega) = T_0 \frac{\sin X}{X}$$

where  $X = \frac{\omega T_0}{2}$ . A model for this source by summing the radiation from two stationary points at the ends gives an approximate waveform

$$f_a(t) = \frac{T_0}{2} \delta\left(t + \frac{T_0}{2}\right) + \frac{T_0}{2} \delta\left(t - \frac{T_0}{2}\right)$$

The Fourier amplitude spectrum for this approximation is

$$F_a(\omega) = T_0 \cos X.$$

At zero frequency both the approximate and the exact spectra have amplitude  $T_0$  and zero slope, but as  $|X|$  increases they diverge. We introduce  $X_s$  as the upper limit on values of  $|X|$  for which  $F_a$  is a satisfactory approximation to  $F_e$ .  $X_s$  should almost certainly be given a value less than 1, for at  $X = 1$ ,  $F_a$  is only about two-thirds of  $F_e$ . For a propagating fault, Ben-Menahem (1961) showed

$$X = \frac{\omega L}{2c} \left( \frac{c}{v} - \cos \theta \right)$$

where  $c$  is the wave propagation speed and  $\theta$  is the angle between the direction of rupture propagation and the direction to the receiver. If  $|X| < X_s$ , then the frequencies  $f$  which are adequately represented are given by

$$f = \frac{\omega}{2\pi} < \frac{c}{\pi L} \frac{X_s}{(c - v \cos \theta)} = f_s.$$

Thus, a more dense grid spacing is needed to obtain displacements at backward angles from the direction of rupture propagation. For the cases of this paper, we use the simplified estimate  $f_s = \frac{\beta}{\pi L}$ , which can be derived using  $X_s$  less than 0.8 for our source receiver geometries. For other cases, particularly where  $\theta > \frac{\pi}{2}$  or for small rupture velocities, the exact formula should be used.

Computer time is in general proportional to  $f_s^3$ . The powers of  $f_s$  arise because the distance  $L$  is used as the spacing of Green's functions on the fault in both coordinate directions. The third power arises because for a larger  $f_s$  the Green's function must be calculated at a greater number of points in time. Here, waves at frequency  $f_s$  are sampled at a rate of six times per cycle.

The effect of  $f_s$  may be illustrated by replacing the Green's function in step 1 with the nonphysical function  $h = \frac{1}{R} H(t - R/c)$ , where  $H$  is the Heaviside step function and  $R$  is the distance between the grid point on the fault and the receiver. The discontinuity in  $h$  is typical of realistic Green's functions. A model is shown in Figure 2, using this function  $h$ , for three values of  $f_s$ . These values

required, respectively, 7, 180, and 2303 total evaluations of  $h$  in space and time. Thus, each successively greater value of  $f_s$  caused over an order of magnitude increase in computer time. The lines beneath the time axis in Figure 2 show the time interval  $T_s = f_s^{-1}$  for each value of  $f_s$ . One obvious inaccuracy is that the computed waves do not begin at the theoretical arrival time shown by the arrow. This discrepancy is inevitable for the case with only one grid point, as that point is not at the origin of rupture. For the other two cases, where a grid point is at the origin of rupture, the discrepancy originates in the numerical second derivative. In all cases, the difference between the time when the computed wave becomes non-zero and the theoretical arrival time is considerably shorter than  $T_s$ . The waveform would not be much different for values of  $f_s$  larger than the largest shown, where the duration of the wave is about four times  $T_s$ .

The integration to evaluate the Green's function in step 1 is the final major source of errors in the computed waveform. This is done in a Romberg integration subroutine (Wilf, 1967), which forms a series of estimates to the integral, doubling the number of points in the integrand for each successive estimate. It uses this series to predict the value of the integral, and returns an answer when two successive predictions differ by less than a specified relative error ( $\epsilon$ , say). In computing the Green's function for a series of times in step 1, the answer for each time could have a random error, or the answers may be systematically

Reproduced from  
best available copy.

too large or too small. Figure 3 shows the effect a large random error may have on the second waveform in Figure 2. To obtain the waveform with errors in Figure 3, each point in time of each of the nine Green's functions was multiplied by a random value between 0.9 and 1.1. The result is quite similar to the answer without errors, indicating that random errors in step 1 have little effect upon the solution.

Numerical evaluation of the integral given by Johnson (1974) to obtain the Green's function often gives a result which is systematically slightly too large or too small. To be sure this systematic effect is negligible, it is necessary to repeat calculations changing only the relative error parameter  $\epsilon$  until the resultant waveform no longer changes when  $\epsilon$  is decreased further toward zero. Such trials indicated that  $\epsilon = 10^{-3}$  is adequate to reliably calculate displacements, but throughout this paper we use  $\epsilon = 10^{-4}$  or smaller.

The half space Green's functions were subjected to several tests, to be sure they are computed correctly. These will now be mentioned briefly before proceeding to some comparisons of half space and infinite space displacements.

1. Displacements agreed with Figures 7, 8, and 9 of Johnson (1974).
2. First motions were in the proper directions.
3. Rayleigh waves have retrograde elliptical particle motion.

4. Symmetry properties: All components of radiation from several sources showed the expected behavior of being either even or odd, depending on the source, in both  $x$  and  $y$ .
5. The static offsets were in accord with results of Sato and Matsuura (1974).
6. Wave equation: Using reciprocity, a Green's function  $\mathcal{E}_{ij,k'}$  will obey the wave equation for a receiver fixed on the free surface when the source location is varied to compute the spatial derivative. As programmed, the terms  $\mathcal{E}_{ij,k'} + \mathcal{E}_{ik,j'}$  in eq. (1) are summed algebraically. For P-waves,  $\mathcal{E}_{ij,k'} = \mathcal{E}_{ik,j'}$ , and computed displacements were shown to obey the wave equation. The S-component lacks this symmetry, and could not be subjected to this test.

The comparison in the next section of half space and infinite space displacements from a point dislocation source may also be regarded as a mutual check of the half space and infinite space calculations.

#### NUMERICAL EXAMPLES: POINT DISLOCATION SOURCES

Dynamic displacements at a distance  $r$  from a point dislocation source in an infinite space consist of five components: two far field terms which decrease as  $r^{-1}$ , two intermediate field terms which decrease as  $r^{-2}$ , and the near field term which decreases as  $r^{-4}$  (Haskell, 1969).

A comparison of motions from a point dislocation in a half space and in an infinite space serves two purposes. First, it shows how well the far field components from a point source in an infinite space (which can be quickly computed) can be corrected using plane wave theory to obtain the corresponding components in the half space. Second, it shows how the near and intermediate field displacements are affected by the free surface.

Displacements were calculated at eight stations, chosen such that in the half space direct rays have angles of incidence (measured from the normal to the surface) which varied from 10 to 30 degrees in 10 degree intervals. We used two sources, both on a vertical fault: one was strike slip and the other was dip slip. The stations are on the  $x_2$  axis, so that far field radiation is entirely SH from the strike slip source, and entirely P-SV from the dip-slip source. Note that the displacements for the SH case cannot be calculated by the source-image method because the dislocation source causes P- and SV-far field motions elsewhere in the  $x_3 = 0$  plane.

From these calculations, the free surface amplification was derived for a far field body wave by dividing the computed amplitude for the half space by the corresponding amplitude for the infinite space case. For P-waves, the

computed ratios are shown in Figure 4, and for SV-waves, these ratios are shown in Figure 5.

The half space SH waves had the same wave shape as the whole space waves, and twice the amplitude, to within 3%. This agrees well with theory, which predicts that exactly twice the amplitude should be expected at all angles of incidence.

For P and SV waves, the theoretical amplification of waves by the free surface is given by equations in the Appendix. Corresponding theoretical curves are plotted in Figure 4 for P-waves and Figure 5 for SV-waves, together with the ratios of the components of motions derived from the model calculations. For P-waves, as discussed by Kawasaki *et al.* (1973), the free surface does not greatly affect the wave shape, and the calculations agree well with the theory.

Because the SV displacements are strongly modified by the free surface, they are shown for both the half space and the whole space in Figure 6 for stations at 30 to 80 degrees. The station at 30 degrees is not beyond the critical angle ( $34.7^\circ$ ), there is no phase shift, and the wave shapes are similar. For the other stations, we must actually apply the theoretical phase shift to determine how well the calculations agree with theory. To evaluate the effect of this phase shift, consider an incident waveform  $f(t)$  with Fourier transform  $F(\omega)$ . The Fourier trans-

form of the surface motion is, using formula A-5 or A-6,  $U(\omega) = R e^{i\delta \text{sgn}(\omega)} F(\omega)$ , where  $R$  is  $|RXS|$  or  $|RZS|$ , and  $\delta \text{sgn}(\omega)$  is the corresponding phase shift. Applying the inverse transform to obtain the surface motion gives:

$$u(t) = \frac{1}{2\pi} \int_{-\infty}^{\infty} R e^{i\delta \text{sgn}(\omega)} F(\omega) e^{i\omega t} d\omega$$

$$= R \cos \delta f(t) + R \sin \delta H(f(t))$$

$$\text{where } H(f(t)) \equiv \frac{1}{\pi} \int_0^{\infty} d\omega \int_{-\infty}^{\infty} f(\tau) \sin \omega (\tau - t) d\tau.$$

The function  $H(f(t))$  is the Hilbert transform of  $f(t)$ , discussed in more detail by Choy and Richards (1975).

The phase shifted, amplitude corrected, whole space SV waves are compared with the half space waves in Figure 7. Except at  $40^\circ$  and  $50^\circ$  the exact wave shapes and amplitudes agree well with those found by applying the plane wave correction. At  $40^\circ$  the displacements show practically no resemblance to each other. At  $50^\circ$  there are lesser differences, and another phase arrives before the SV-wave. This is the SP-phase. At  $40^\circ$ , this phase is superimposed on the S-wave, and is perhaps the sole cause of the disagreement. Although for angles greater than  $50^\circ$  the SP-phase has moved out of the time window in Figure 7, it

appears out to  $80^\circ$ , with a shape similar to the SP-phase at  $50^\circ$ , but decreasing amplitudes relative to the S-wave. As at  $40^\circ$  and  $50^\circ$ , amplitudes of the SP-phase may be larger than the S-wave, but in Figure 7 it appears to be depleted in high frequencies relative to the S-wave.

The second objective of comparing displacements from a point dislocation in a half and an infinite space was to study the amplification of near and intermediate field components. These displacements cannot be separated for individual study as were the far field terms. But at times when far field terms are absent, the ratios of the half space to the infinite space displacements reveal the net effect of the free surface upon any near field or intermediate field terms which are present. This net effect is complex, and in general is not well described by the approximation that the free surface causes the amplitudes to double.

Because the stations are on the  $x_2$  axis (Figure 1, Figure 6 caption), the SH case causes only  $U_1$  displacements and the P-SV case causes only  $U_2$  (horizontal) and  $U_3$  (vertical) displacements. In speaking of the near and intermediate field terms, it is better to refer only to the  $U_1$ ,  $U_2$  and  $U_3$  components to remove the connotation of phases travelling only with the P- and S-velocities.

Immediately after the P-wave, the amplitude ratio for each component resembles the amplitude ratio for the horizontal component of the P-wave (Figure 4). Just before

Reproduced from  
best available copy.



the S-wave, the ratio for each component, where it could be measured, had increased to a value generally in the range of 2.5 to 2.8. This ratio could not be measured for the  $U_2$  and  $U_3$  components incident at angles greater than 30 degrees because in these cases the SP-wave and the phase shift of the S-wave also cause displacements in the half space before the theoretical S-wave arrival time.

The static offset ratios for all three components, shown in Figure 8, generally differ from 2.0. These ratios, like the ratios of far field components, are independent of the distance between the source and the station. For angles of incidence less than 30 degrees these ratios differ considerably from the amplification ratios of far field body waves. Thus, it appears that even when the dynamic displacements of the surface of a half space can be approximated by twice the infinite space displacements, the static displacements cannot be reliably approximated in this way.

In summary, the amplification and phase shift of the far field components of displacement close to a point dislocation can be understood well by applying plane wave theory. The theoretical amplification of plane waves does not apply to the static offset or to the amplification of near field components of dynamic displacements, and it cannot, of course, explain the SP-phase or the Rayleigh wave.

## NUMERICAL EXAMPLES: EXTENDED DISLOCATION SOURCES

For a small earthquake (resembling a point source), Figures 4-7 show that doubling infinite space motions is inadequate for stations with an angle of incidence of over 30 degrees if there is any SV motion, and nearly always inadequate if the angle of incidence is greater than 70 degrees. For an extended source, however, the contribution from each Green's function is only a small part of the total motion at the station. Therefore Figures 9-13 were drawn to study half space and whole space motions for extended vertical faults. The fault motion is dip slip for the models in Figures 9 and 10, so that SV motion dominates, and strike slip for the models in Figures 11-13, so that SH motion dominates. The angles of incidence from the major fraction of fault planes are in three ranges: 30-60° (Figures 9 and 11), 60-80° (Figures 10 and 12), and over 80° (Figure 13). In these cases, waveforms are low pass filtered with a corner at  $f_g$  to diminish higher frequency noise such as shown in Figure 2.

Half space motions are different from the doubled whole space motions for the dip slip fault (Figures 9, 10). In going to higher angles of incidence, the relative amount of SV motion increases and the whole space motions agree less with the half space motions. The static offsets, determined by the last value each component attains, gen-



erally differ between the models. A dislocation in an infinite space to model the motions in the half space would probably not have rupture parameters similar to those used to calculate the half space motions.

For the strike slip faults (Figures 11-13), the horizontal displacements (including the static offset) derived from the whole space model resemble fairly well the half space motions, with the exception of the clear Rayleigh wave on the  $u_1$  component in Figure 13. At 60-80 degrees, which contains less P-SV motions than 30-60 degrees, the doubled whole space motions approximate the half space motions better than at 30-60 degrees. Above 80 degrees, the Rayleigh wave causes the agreement to worsen. The vertical ( $u_3$ ) components are similar in Figure 11, but in Figures 12 and 13 they are not. The horizontal static offsets from the whole space models match the static offsets of the half space models. This is not expected considering the offsets for point sources shown in Figure 8. A dislocation model in an infinite space would have similar rupture parameters to those used to calculate the half space motions, providing the vertical component was ignored where appropriate.

The  $u_1$  and  $u_3$  components in Figure 13 show a strong Rayleigh wave, clearly identified by comparison with the whole space model. Pekeris and Lifson (1957) showed that for distances  $r$  and source depths  $z$ , the Rayleigh wave is emerging for  $r/z = 5$  and clearly seen for  $r/z = 10$ . These

ratios correspond to angles of incidence of about 79 and 84 degrees respectively. Thus, Figures 9-12 do not show a Rayleigh wave.

The Parkfield and San Fernando earthquakes have been studied extensively using high quality, close distance accelerograms to derive source dislocation models. Table I presents the fraction of the faults for these two cases which give direct ray angles to the accelerograph in the ranges 0-30, 30-60, 60-80 and 80-90 degrees. These percentages are estimated for a fault in a homogeneous half space using the geometry of Trifunac (1974) for the San Fernando earthquake and of Anderson (1974) for the Parkfield earthquake. Even at the closest stations to the fault, at most about 20% of the fault is in the 0-30 degree range. The remaining 80% of the fault, including the epicenters, is in the range where the free surface may significantly distort the waveform derived from the whole space approximation. The San Fernando earthquake had a thrusting mechanism while the Parkfield earthquake had a strike slip mechanism, and thus S-waves from the San Fernando earthquake at nearby stations would in general have a greater component of SV type motion. Therefore, when the infinite space method is used, rupture parameters derived for the San Fernando earthquake are more likely to be incorrect than rupture parameters derived for the Parkfield earthquake.

Table 1 indicates that even at the best placed instruments, angles of incidence are likely to be high for most

of the fault plane. This is especially indicated by the angles of incidence of the Pacoima Dam accelerograph. In this case, the instrument was located directly above the fault, and yet SV-type waves from only about 20% of the fault plane would be relatively undistorted by the free surface.

### CONCLUSIONS

A practical way of computing displacements on the surface of a half space is by a two step process. The first step is calculating and storing the Green's function for a given station for a grid of points on the fault; and the second step is convolving with the source time function. In studying a particular accelerogram record, this method is far more economical than it would be to recompute the Green's functions for each trial source function. This two step method also gives a clear idea of what frequencies are significant in the calculated displacement record.

The dynamic displacement of the surface of a half space caused by an extended dislocation source generally differs from two times the displacement which would result from the same source in an infinite space. There are two exceptions.

The first exception is a fault located such that angles of incidence at the station are less than 30 degrees from vertical. For a large fault, however, even at the best placed instruments, the angles of incidence will be this small from only a small fraction of the fault. This case

is therefore most useful for studying small earthquakes. The static offset estimated from the infinite space method may be wrong in this case, but this is not of practical importance as most data cannot resolve such offsets.

The second exception occurs when the motion at the source is predominantly strike slip. Then the horizontal components may be modeled by the infinite space motion when the Rayleigh wave is not important (eg. for angles of incidence less than  $80^\circ$ ). The vertical component in this case may also be used for angles of incidence less than about 60 degrees. This case will be most useful for studying strike-slip earthquakes.

In many cases, a small earthquake recorded at a large angle of incidence can be modeled using the infinite space method. When the observed S-wave is separated from other phases, and near field terms are small, it can be separated into SV- and SH- components. Then the phase shift and amplitude correction can be applied to each component separately to obtain the incident waveforms, for comparison with infinite space models.

Reproduced from  
best available copy.

#### ACKNOWLEDGMENTS

F. C. Richards, L. D. Alsop and J. Rife critically reviewed the manuscript. H. Nagoe and G. Anderson helped with the drafting. Computer time was supplied by the Goddard Institute of Space Studies in New York City. This research was supported by the Advanced Research Projects Agency of the Department of Defense, and was monitored by the Air Force Office of Scientific Research under Contract W. 33-623-74-C-0023.

## APPENDIX 1

*Derivation of Amplification Coefficients  
for Body Waves Incident on a Free Surface*

The ratio of the amplitude of each component of the free surface motion to the amplitude of the same component of an incident body wave is derived here. Knopoff *et al.* (1957), who derive the ratio of each component to the total amplitude of the incident wave, have some misprints which make this derivation necessary. In eq 6, a quantity they refer to as  $\tanh \theta'$  is always greater than 1; in eq 7, the phase is incorrect in the center of the three equalities because  $\tan 2\phi$  changes sign at  $45^\circ$ ; and in eq 9 (substituting " $\tanh \theta'$ " as defined), the phase does not agree with Figure 3. The figures in Knopoff *et al.* are correct. The closely related equations for reflection and transmission coefficients at a boundary between two layers have a long history of published errors (Hales and Roberts, 1974).

We first discuss the problem of a plane P-wave incident with angle  $i$  and a plane SV-wave incident at angle  $j$ ; both incident from  $z < 0$  on a free surface  $z = 0$ ; and both waves having horizontal slowness  $s$ . Later, we will specialize to the case where only one of these waves is incident.

The total wave field is described by displacement

$$\underline{u} = \text{grad } \phi + \text{curl } (0, \Psi, 0) = \left( \frac{\partial \phi}{\partial x} - \frac{\partial \Psi}{\partial z}, 0, \frac{\partial \phi}{\partial z} + \frac{\partial \Psi}{\partial x} \right)$$

where

$$\begin{aligned} \phi &= P_i f\left(t - sx - z \frac{\cos i}{\alpha}\right) + P_r f\left(t - sx + z \frac{\cos i}{\alpha}\right) \\ &= \phi_i \qquad \qquad \qquad + \phi_r \end{aligned}$$

$$\Psi = S_i f\left(t - sx - z \frac{\cos j}{\beta}\right) + S_r f\left(t - sx + z \frac{\cos j}{\beta}\right)$$

Here the first term on the right represents the incoming wave in each case, and the second term represents the outgoing reflected wave. In these equations  $f(t)$  denotes the time dependence of the potentials,  $s = \frac{\sin i}{\alpha} = \frac{\sin j}{\beta}$  is the horizontal slowness,  $\alpha$  is the P-wave velocity, and  $\beta$  is the S-wave velocity. The terms  $P_i$  and  $S_i$  are constants, and  $P_r$  and  $S_r$  are unknowns to be derived from the free surface boundary conditions of zero traction on  $z = 0$ .

These boundary conditions yield the equations:

$$(P_i - P_r) \frac{\sin 2i}{\alpha^2} - (S_i + S_r) \frac{\cos 2j}{\beta^2} = 0$$

$$(P_i + P_r) \cos 2j + (S_i - S_r) \sin 2j = 0,$$

which have the solution

$$P_r = P_i \left( \frac{1}{D} \right) \left( \frac{\sin 2i \sin 2j}{\alpha^2} - \frac{\cos^2 2j}{\beta^2} \right) + S_i \frac{1}{D} \left( -2 \frac{\sin 2j \cos 2j}{\beta^2} \right)$$

$$S_r = P_i \left( \frac{1}{D} \right) \left( 2 \frac{\sin 2i \cos 2j}{\alpha^2} \right) + S_i \frac{1}{D} \left( \frac{\sin 2i \sin 2j}{\alpha^2} - \frac{\cos^2 2j}{\beta^2} \right)$$

$$\text{where } D = 2s \frac{\cos i \sin 2j}{\alpha} + \frac{1}{\beta^2} \cos^2 2j$$

The desired ratios are the amplitude of a component of the motion of the free surface ( $z = 0$ ) due to either an incident P-wave ( $S_i = 0$ ) or SV-wave ( $P_i = 0$ ) divided by the same component of motion which would take place if the surface were absent. For example,

$$RXP = \frac{u_x^p(\frac{1}{2})}{u_x^p(\infty)} = \frac{\{-P_i s - P_r s - S_r \frac{\cos j}{\beta}\}}{-P_i s}$$

Here  $u_x^p$  refers to the horizontal ( $x$ ) component of P-wave motion, and the  $(\frac{1}{2})$  or  $(\infty)$  refer to the case of a half space and of an infinite space respectively.

For incident P-waves, the ratios are:

$$RXP = \frac{2 \sin 2i \cot j}{\alpha^2 D} \quad (A-1)$$

$$RZP = \frac{2 \cos 2j}{\beta^2 D} \quad (A-2)$$

For S-waves incident at angles less than the critical angle  $j_c$  ( $\sin j_c = \frac{\beta}{\alpha}$ ), the ratios are:

$$RXS = \frac{2 \cos 2j}{\beta^2 D} \quad (A-3)$$

$$RZS = \frac{4s \cos i \cot j}{\alpha D} \quad (A-4)$$

For S-waves incident at angles greater than critical, a phase shift is introduced. At this point, it is necessary to consider a specific frequency component:  $f(t) = e^{i\omega t}$ . Then for  $j > j_c$  the quantity  $\frac{\cos i}{\alpha}$  is replaced by an imaginary quantity  $-ib \operatorname{sgn}(\omega)$ , where the sign is chosen so that the potential  $\phi_r$  will decrease with increasing distance from the free surface. Here  $\operatorname{sgn}(\omega) = 1$  if  $\omega > 0$  and  $-1$  if  $\omega < 0$ , and  $b = \sqrt{s^2 - \alpha^{-2}}$ . Then the ratios for  $j > j_c$  are:

$$RXS = \left| \frac{2 \cos 2j}{\beta^2 D'} \right| e^{i(p + \theta)} \quad (A-5)$$

$$RZS = \left| \frac{4 s b \cot j}{D'} \right| e^{i(p - \frac{\pi}{2} \operatorname{sgn}(\omega))} \quad (A-6)$$

where

$$D' = \left[ \left( \frac{\cos 2j}{\beta} \right)^2 + (2 s b \sin 2j)^2 \right]^{1/2}$$

$$\tan p = \frac{2\beta^2 sb \sin 2j}{\cos^2 2j} \operatorname{sgn}(\omega_0)$$

$$\text{and } \theta = \begin{cases} 0 & j_c < j \leq \pi/4 \\ \pi & \pi/4 < j < \pi/2 \end{cases}$$

## REFERENCES

- Anderson, J. (1974). A dislocation model for the Parkfield earthquake, Bull. Seism. Soc. Amer., 64, 671-686.
- Anderson, J. G. and P. G. Richards (1975). Comparison of strong ground motion from several dislocation models, Geophys. J. Roy. Astr. Soc., 42, 347-373
- Ben-Menahem, A. (1961). Radiation of seismic surface waves from finite moving sources, Bull. Seism. Soc. Am., 51 401-435.
- Burridge, R. and L. Knopoff (1964). Body force equivalents for seismic dislocations, Bull. Seism. Soc. Am., 54, 1875-1885.
- Choy, G. L. and P. G. Richards (1975). Pulse distortion and Hilbert transformation in multiply reflected and refracted body waves, Bull. Seism. Soc. Am., 65, 55-70.
- Hales, A. L. and J. L. Roberts (1974). The Zoepritz amplitude equations: more errors, Bull. Seism. Soc. Am., 64, 285.
- Haskell, N. A. (1969). Elastic displacements in the near-field of a propagating fault, Bull. Seism. Soc. Am., 59, 865-908.
- Johnson, L. R. (1974). Green's function for Lamb's problem, Geophys. J. R. Astr. Soc., 37, 99-131.
- Kanamori, H. (1972). Determination of effective tectonic stress associated with earthquake faulting. The Tottori earthquake of 1943, Phys. Earth Planet. Interiors, 5, 426-434.

- Kawasaki, I., Y. Suzuki and R. Sato (1973). Seismic waves due to a shear fault in a semi-infinite medium. Part I: Point sources, J. Phys. Earth, 21, 251-284.
- Knopoff, L., R. W. Fredricks, A. F. Gangi and L. D. Porter (1957). Surface amplitudes of reflected body waves, Geophysics, 22, 842-847.
- Pekeris, C. L. and H. Lifson (1957). Motion of the surface of a uniform elastic half space produced by a buried pulse, J. Acoust. Soc. Am., 29, 1233-1238.
- Sato, R. and M. Matsuura (1974). Strains and tilts on the surface of a semi-infinite medium, J. Phys. Earth, 22, 213-221.
- Trifunac, M. D. (1974). A three-dimensional dislocation model for the San Fernando, California, earthquake of February 9, 1971, Bull. Seism. Soc. Am., 64, 149-172.
- Trifunac, M. D. and F. E. Udvardia (1974). Parkfield, California, earthquake of June 27, 1966: A three dimensional moving dislocation model, Bull. Seism. Soc. Am., 64, 511-533.
- Wilf, H. S. (1967). Advances in numerical quadrature, in Mathematical Methods for Digital Computers, Vol. II, A. Ralston and H. S. Wilf, ed., John Wiley and Sons, Inc., New York, 133-137.

TABLE I  
 ESTIMATED FRACTION (NEAREST 5 PERCENT) OF FAULT AREA  
 WITHIN EACH RANGE OF ANGLE OF INCIDENCE

Earthquake/Station	ANGLE OF INCIDENCE (degrees)			
	0°-30°	30°-60°	60°-80°	80°-90°
<u>Parkfield</u>				
Cholame-Shandon #2	10	20	50*	20
Cholame-Shandon #5	0	25	55*	20
Cholame-Shandon #8	0	15	65*	20
Cholame-Shandon #12	0	5	65*	30
Temblor	0	10	60*	30
<u>San Fernando</u>				
Pacoima Dam	20	45*	25	10
Castaic Old Ridge Route	0	0	15*	85
Palmdale Fire Station	0	0	20*	80
Jet Propulsion Laboratory	0	0	45*	55
8244 Orton Blvd.	0	0	75*	25

\*The epicenter is in this range

## FIGURE CAPTIONS

Figure 1: Coordinate system and faulting parameters. The plane  $x_3 = 0$  is the free surface. The fault strikes in the  $x_1$  direction, and the dip  $\delta$  is measured from the horizontal plane. The point  $(x_1, x_2, x_3) = (0, 0, d)$  is the geometrical center of the fault, and the origin of the  $(\xi_1, \xi_2)$  coordinates (not shown) which describe a point on the fault plane. The direction of slip on the fault is given by the unit vector  $\bar{S}$ , with components  $S_1$  (in the  $\xi_1$  direction) and  $S_2$  (in the  $\xi_2$  direction) giving respectively the relative amplitudes of strike slip and dip slip motion.

Figure 2: A model evaluated using three values of  $f_s$ , with the Green's function in step 1 replaced by the non-physical function  $h = \frac{1}{R} H(t-R/\alpha)$  (see text). The table gives the values of  $f_s$  (in Hz.), and the corresponding number of time points, grid points, and total points at which the function  $h$  was evaluated. For each calculation, the line beneath the time axis has a length  $T_s = f_s^{-1}$ . For this calculation  $(x_1, x_2) = (0.866 \text{ km}, 0.5 \text{ km})$ ,  $d = 0.5 \text{ km}$ ,  $\delta = 90^\circ$ . The rupture model is

a propagating ramp with  $L_1 = 1.0$  km,  $L_2 = 1.0$  km,  $v = 3.0$  km/sec,  $\tau = 0.2$  sec.

Figure 3: The effect of introducing a 10% random error to each of the 180 evaluations of  $h$  (in space and time) in the second case of Figure 2.

Figure 4: Theoretical ratios (solid lines) of the amplitude of vertical and horizontal components of P-waves on a free surface to the amplitudes of the same component of the incoming wave (see appendix equations A-1 and A-2). The angle of incidence is measured from the normal to the surface. The data points are these ratios derived from computations with a point source Green's function.

Figure 5: Same as Figure 6 for SV-waves (Appendix equations A3-A6). The computed waveforms for  $30^\circ$  to  $80^\circ$  are shown in Figure 6.

Figure 6: Vertical ( $u_3$ ) and horizontal ( $u_2$ ) components of SV-waveforms for a half space (solid) and an infinite space (dotted) from a point source. For the source,  $d = 10.0$  km,  $(S_1, S_2) = (0, S)$ , and  $\delta = 90^\circ$ . The stations are at  $(x_1, x_2) = (0 \text{ km}, 10 \tan(\text{angle of incidence}) \text{ km})$ . The source has a rise time = 0.1 sec.

Figure 7: Similar to Figure 6, but the free surface amplitude and phase corrections for plane SV-waves (eqs. A-5 and A-6) have been applied to the infinite space waveforms. In some cases,

the infinite space waveform has also been arbitrarily shifted up or down. This is justified because near field components are not amplified the same as the far field SV-waves compared here. Where shifted, the dotted lines which are disconnected from the S-wave (as at  $80^\circ$ ) show the zero for the whole space waveform.

Figure 8: Ratio of static offsets in a half space to those in a whole space for a point source with depth  $d = 10$  km, and at stations  $(x_1, x_2) = (0 \text{ km}, 10 \tan(\text{angle of incidence}) \text{ km})$ . The  $u_1$  component is derived for the source  $(S_1, S_3) = (S, 0)$ ; the  $u_2$  and  $u_3$  components are derived for the source  $(S_1, S_3) = (0, S)$ . The lines only connect points derived from the models.

Figure 9: Comparison of half space (solid line) and doubled whole space (dotted line) displacements for the dip slip fault with  $d = 3.8$  km,  $(x_1, x_2) = (5.0 \text{ km}, 1.5 \text{ km})$ ,  $\delta = 90.0^\circ$ ,  $(S_1, S_3) = (0, S)$ . Rupture parameters are  $L_1 = 5.0$  km,  $L_3 = 3.3$  km,  $v = 3.0$  km/sec, and  $\tau = 1.0$  sec. The vertical scale is in units of  $D_0$  and the time scale is in seconds.

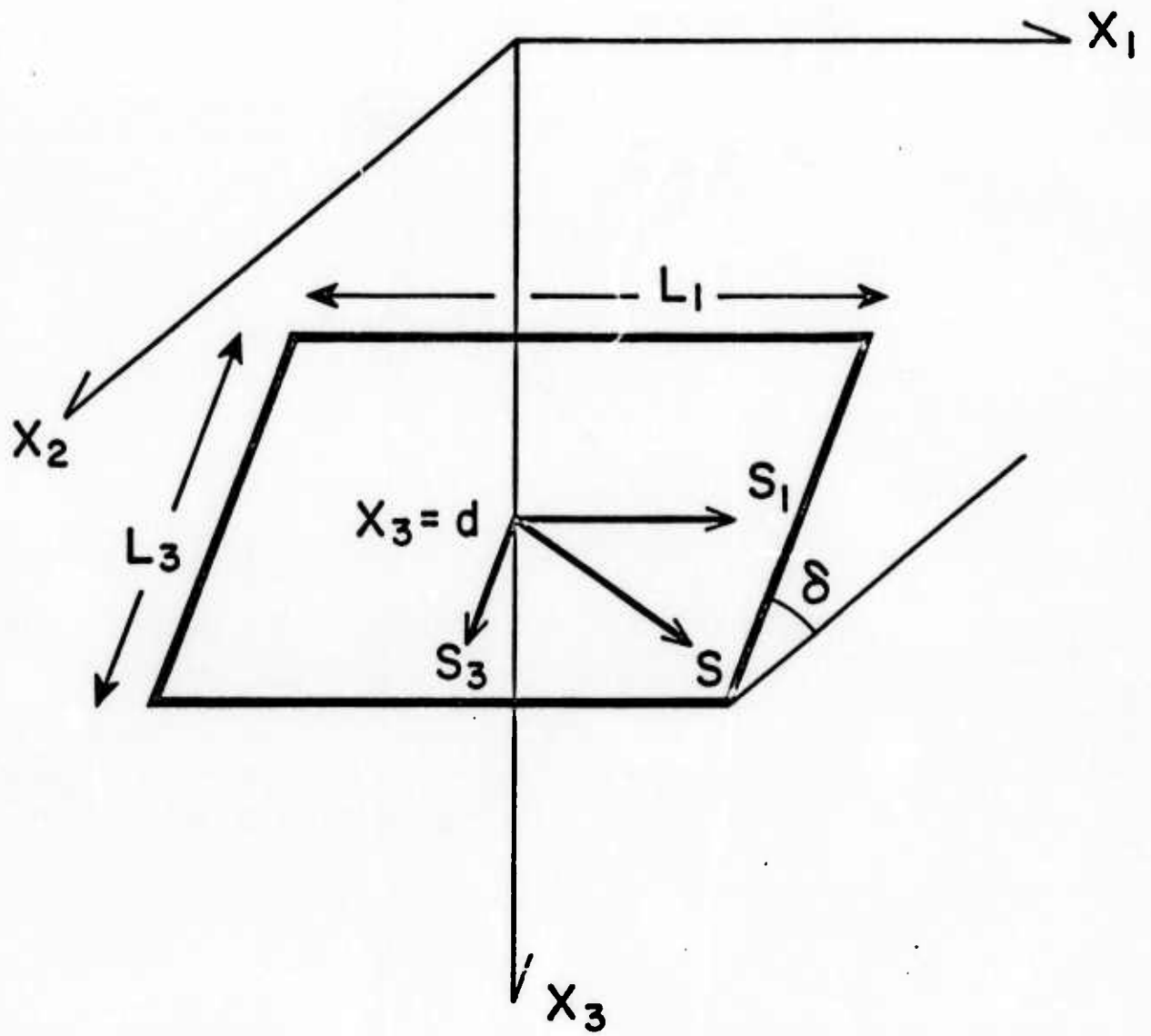
Figure 10: Comparison of half space (solid line) and doubled whole space (dotted line) displacements for the dip slip fault with  $d = 1.1$  km,  $(x_1, x_2) = (5.0 \text{ km}, 1.5 \text{ km})$ ,  $\delta = 90.0^\circ$ ,  $(S_1, S_3) = (0, S)$ . Rupture parameters are  $L_1 = 5.0$  km,  $L_3 = 1.2$  km,

$v = 3.0$  km/sec,  $\tau = 1.0$  sec. The vertical scale is in units of  $D_0$  and the time scale is in seconds.

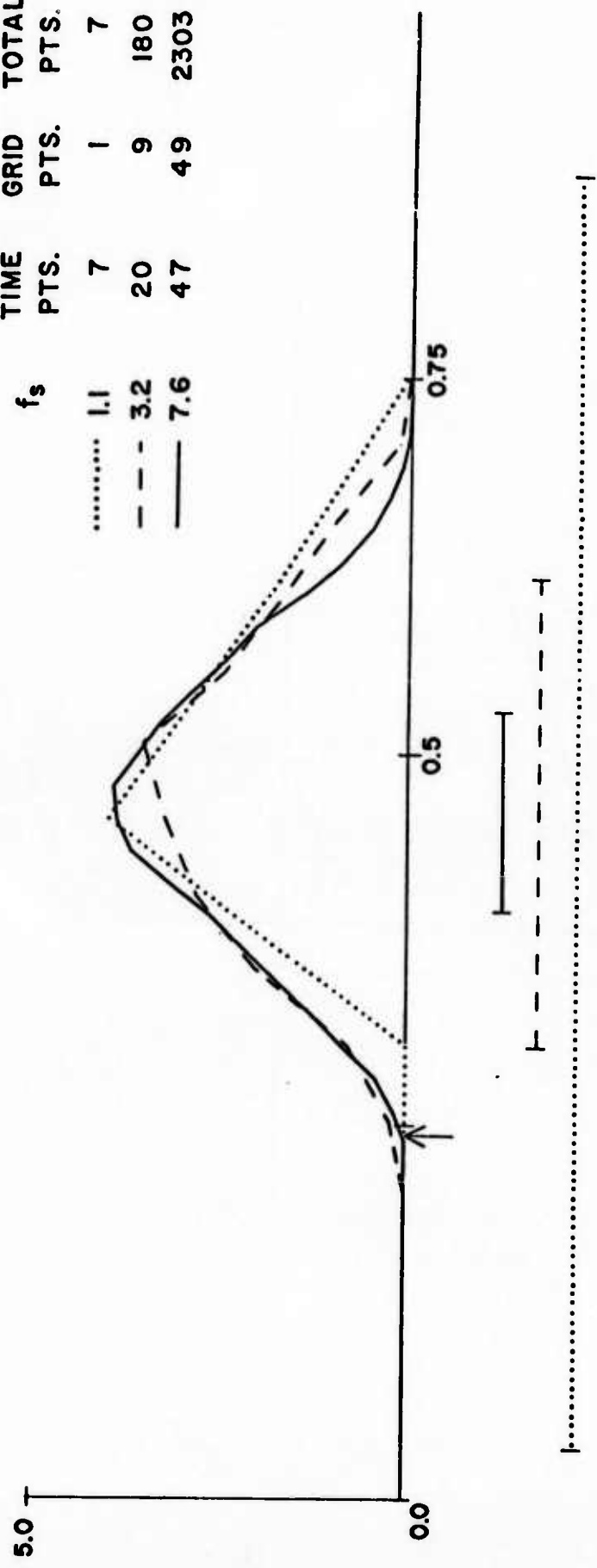
Figure 11: Same as Figure 9, but here for a strike slip fault with  $(S_1, S_3) = (S, 0)$ .

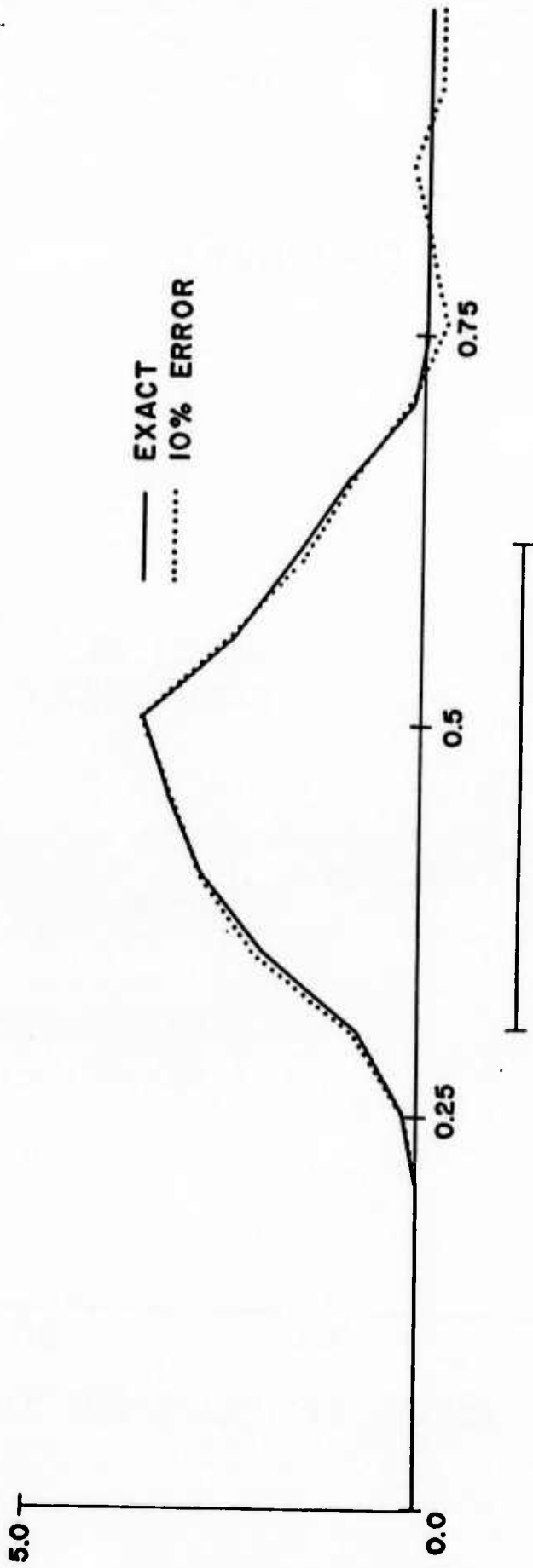
Figure 12 Same as Figure 10, but here for a strike slip fault with  $(S_1, S_3) = (S, 0)$ .

Figure 13: Half space (solid line) and doubled whole space (dotted line) displacements for the strike slip fault with  $d = 0.5$  km,  $(x_1, x_2) = (10.0$  km,  $5.45$  km),  $\delta = 90^\circ$ ,  $(S_1, S_3) = (S, 0)$ . Propagating ramp model parameters are  $L_1 = 10.0$  km,  $L_3 = 0.5$  km,  $v = 3.0$  km/sec,  $\tau = 1.0$  sec. The vertical scale is units of  $D_0$  and the time scale is in seconds.

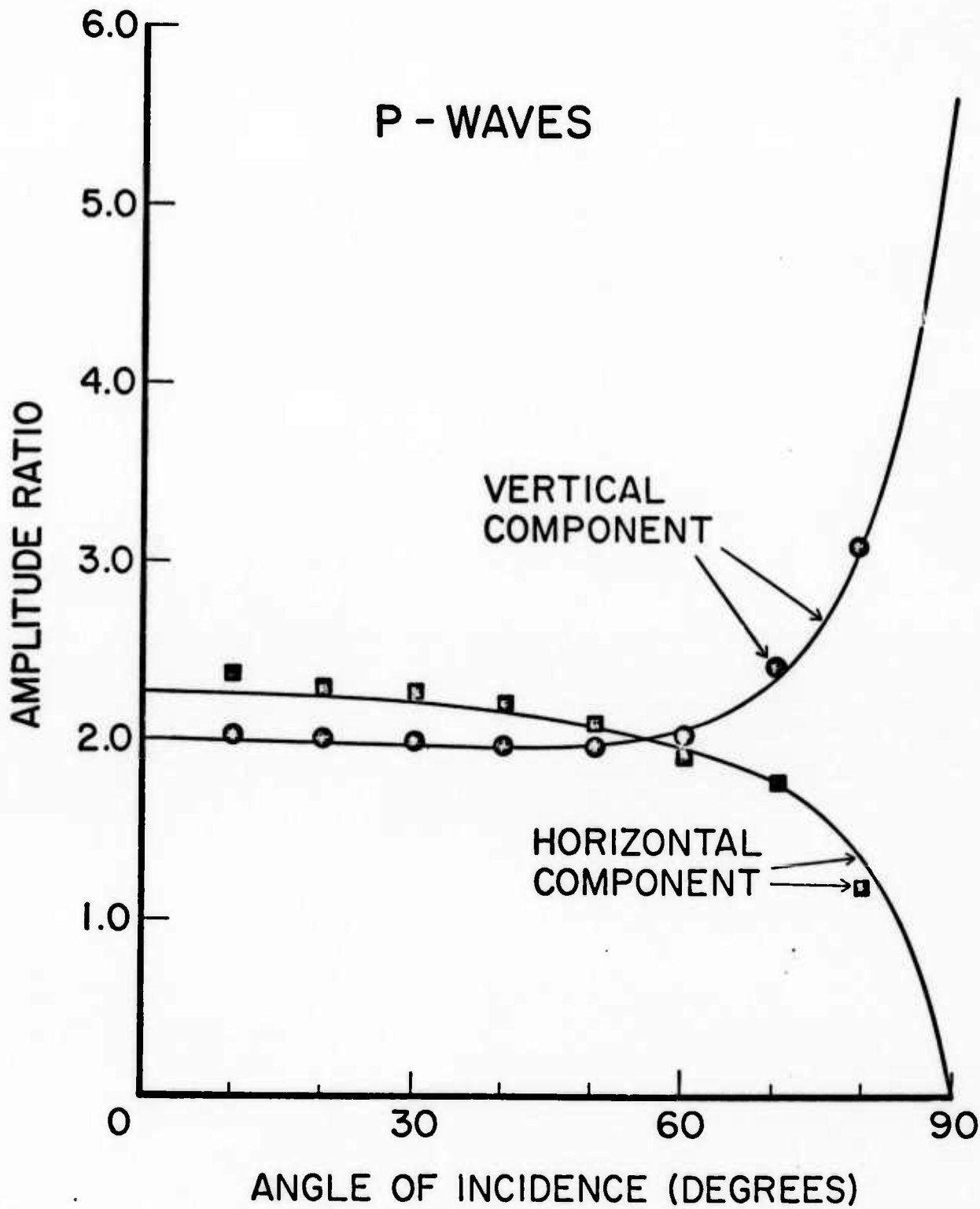


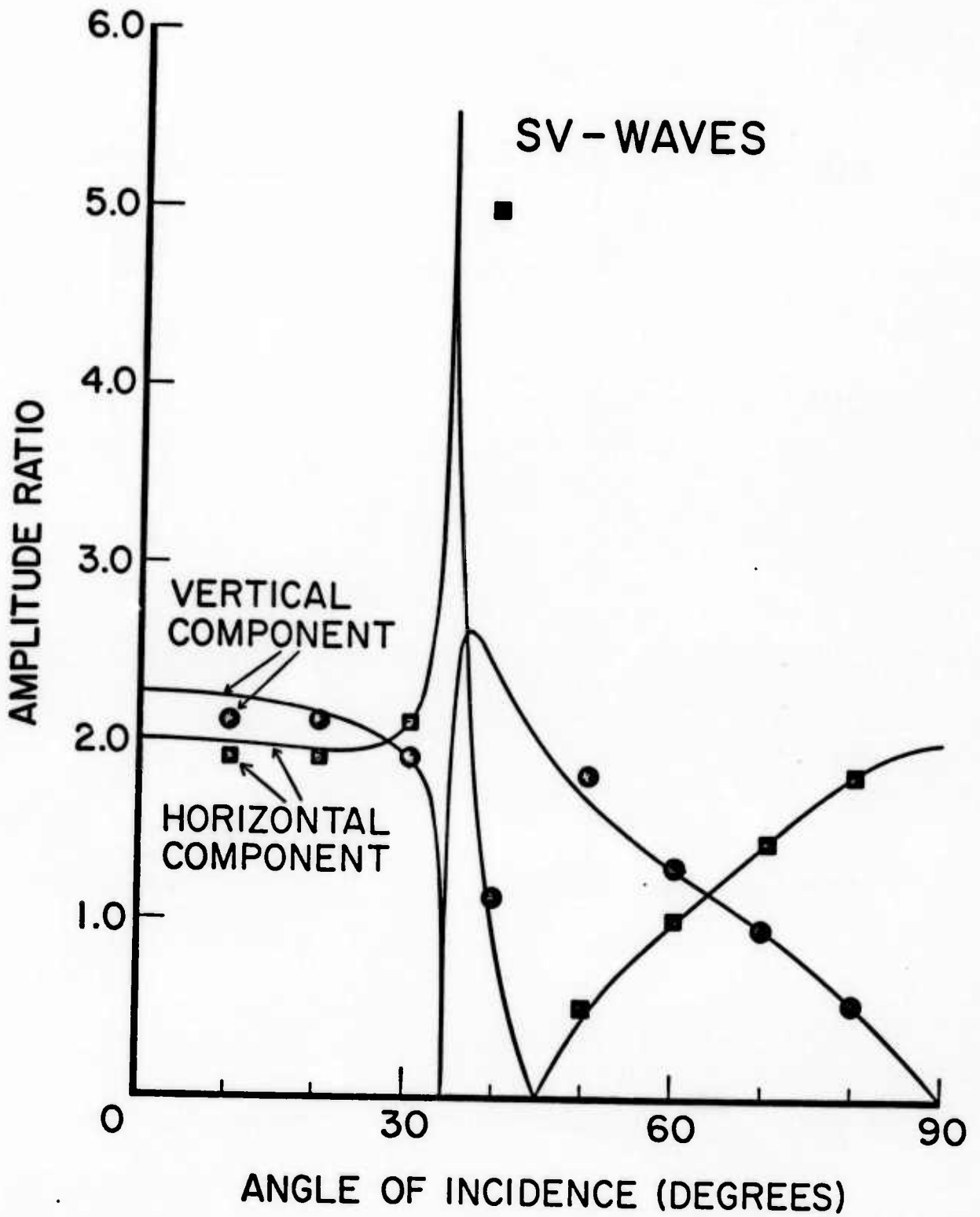
$f_s$	TIME PTS.	GRID PTS.	TOTAL PTS.
.....	7	1	7
- - -	20	9	180
—	47	49	2303





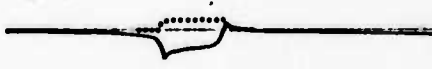
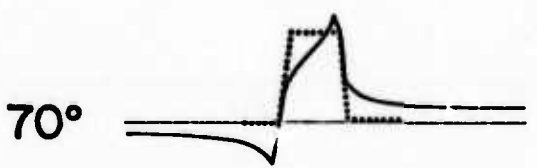
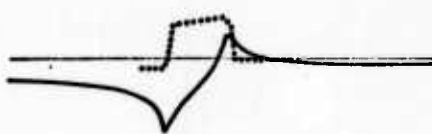
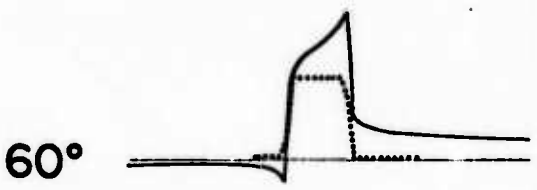
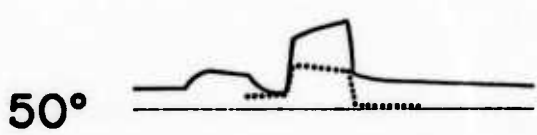
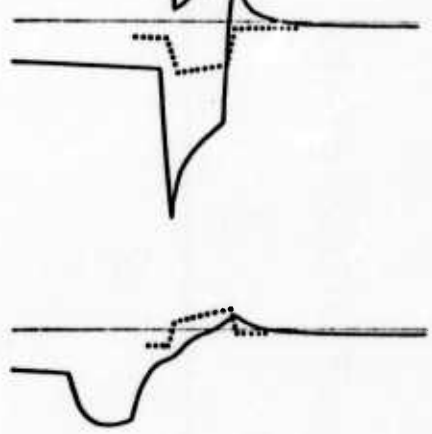
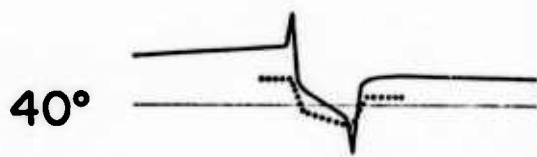
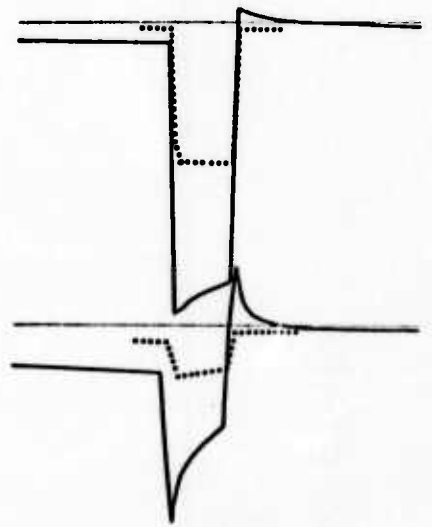
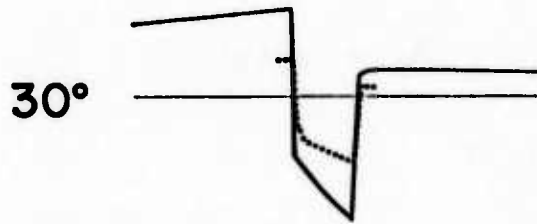
374





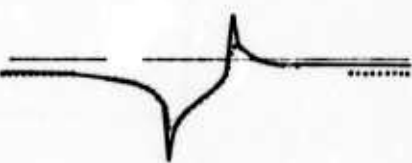
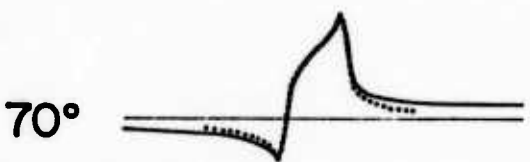
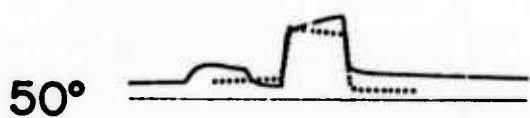
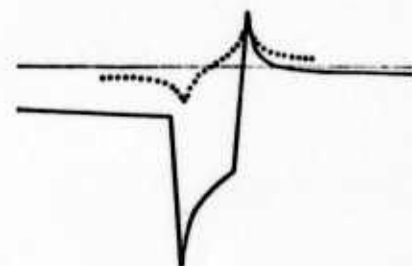
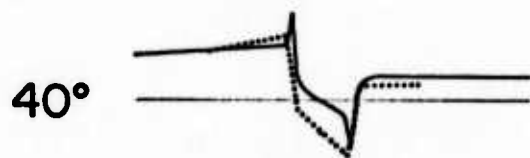
$U_3$

$U_2$

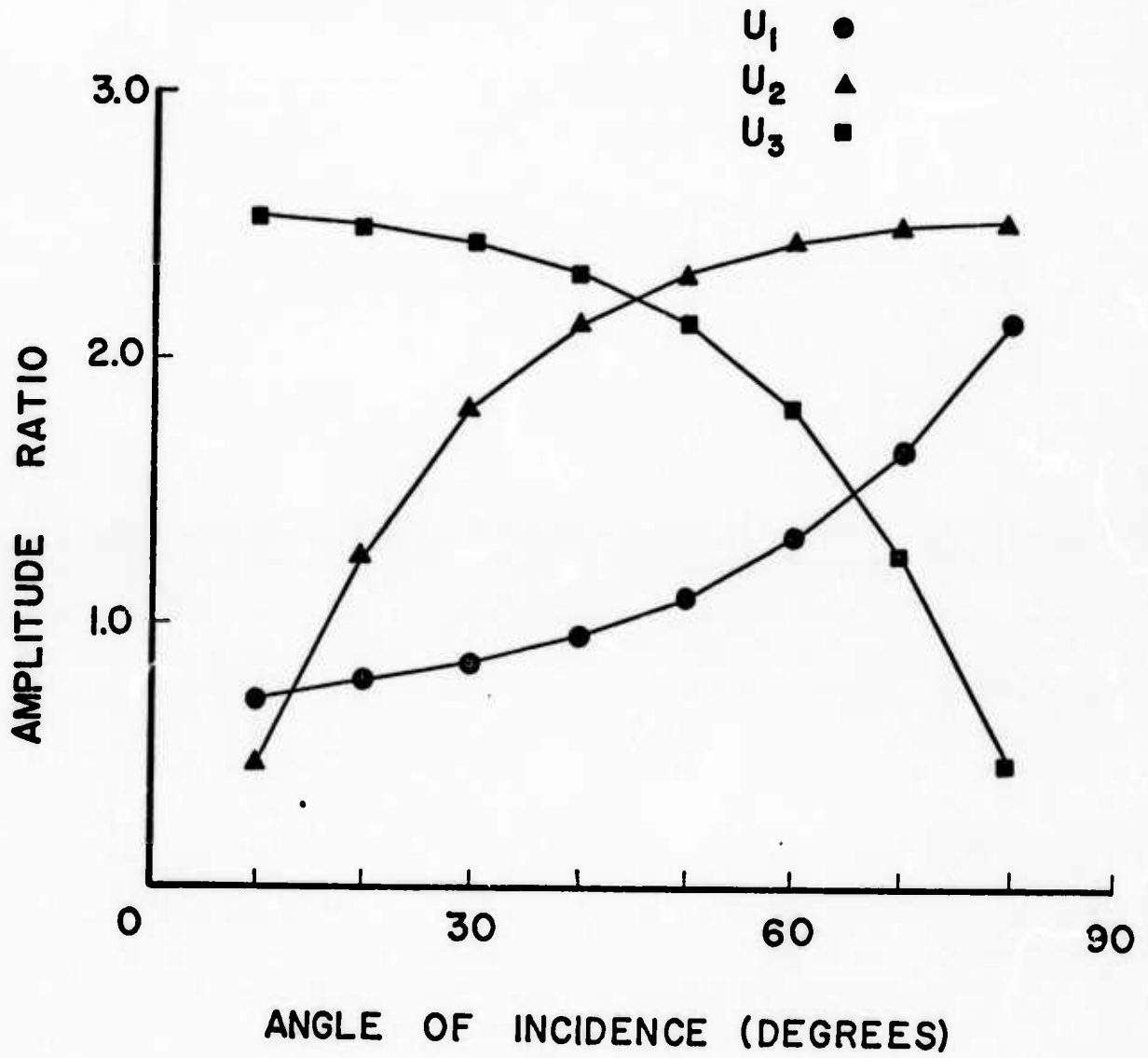


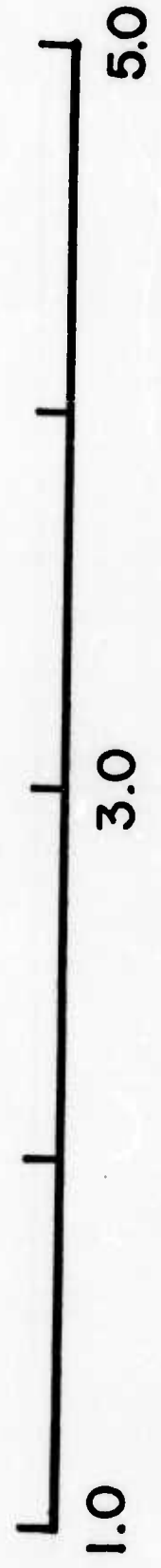
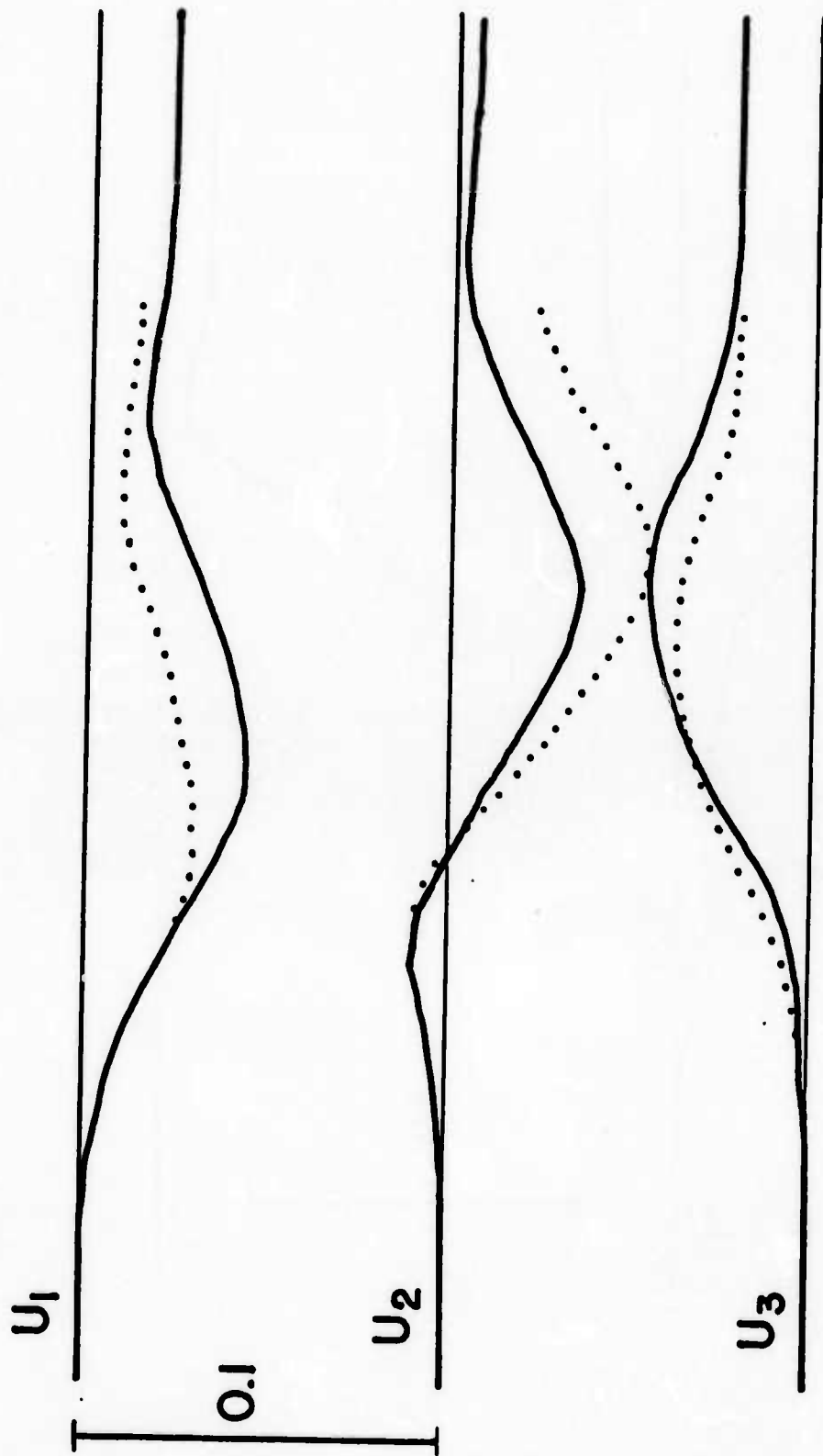
$U_3$

$U_2$

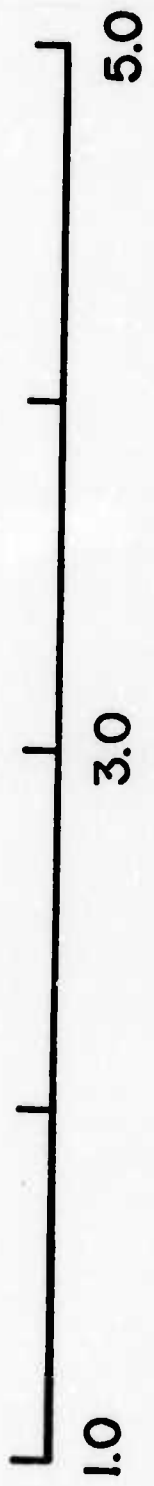
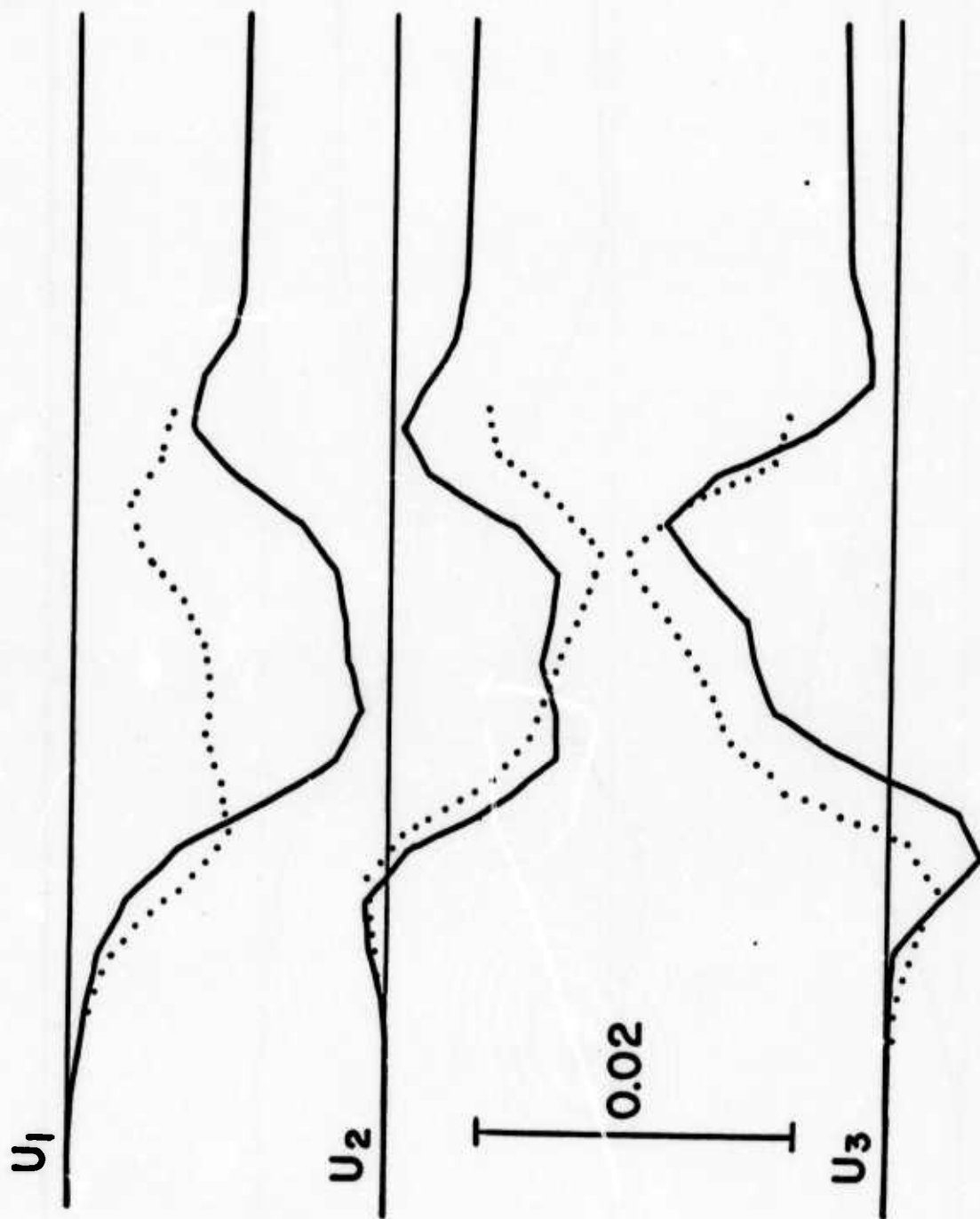


STATIC OFFSETS



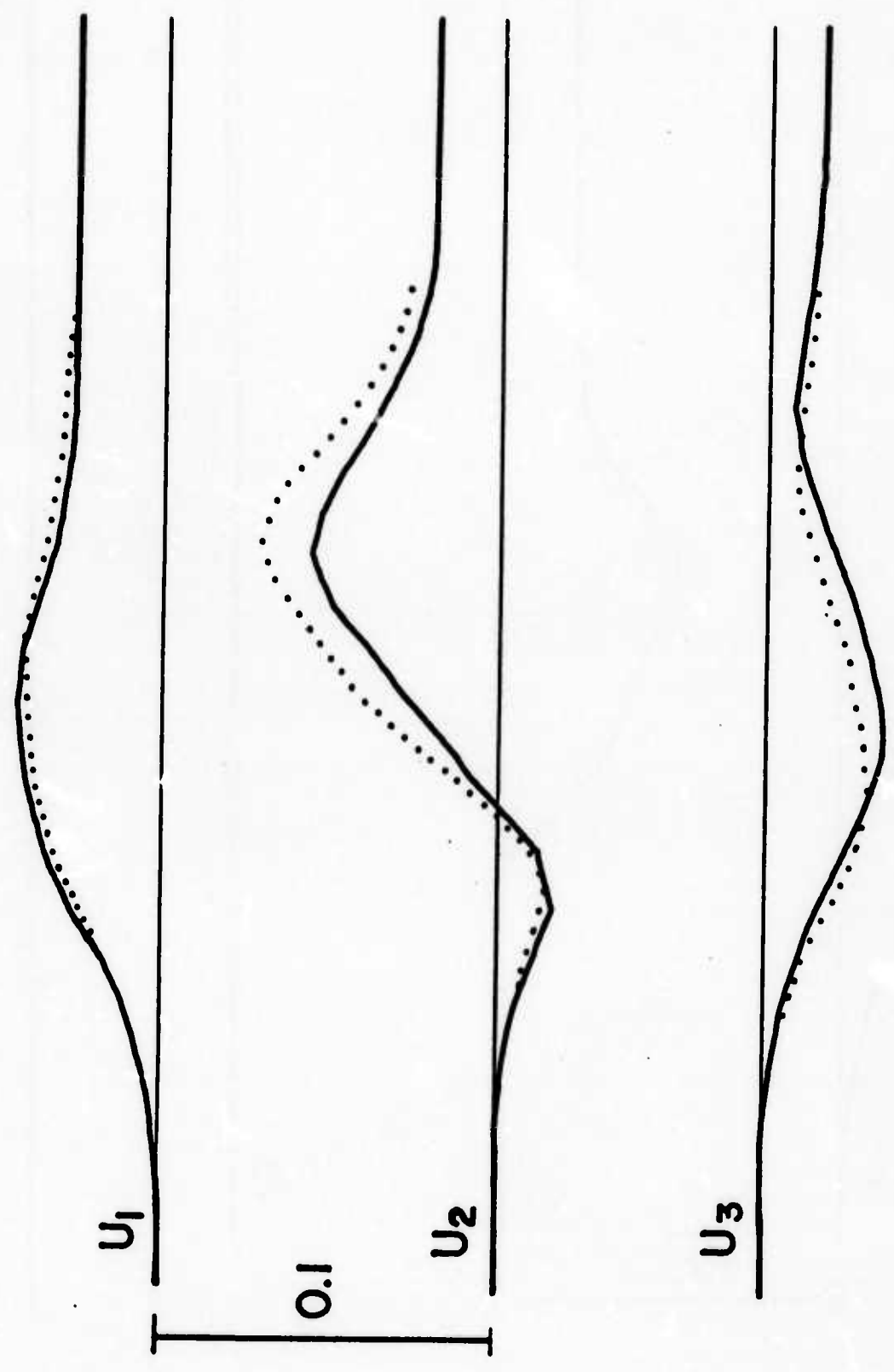


43A



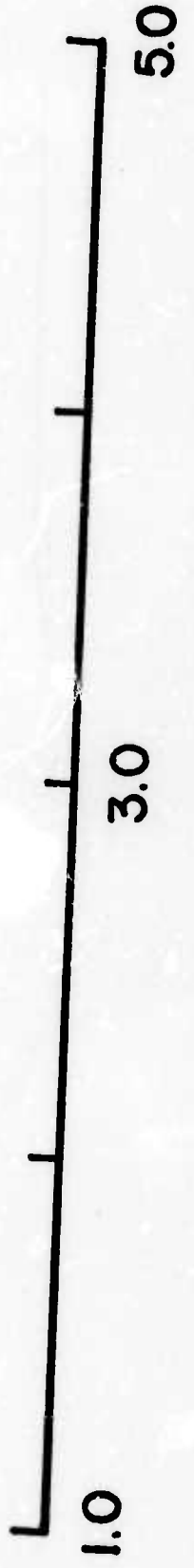
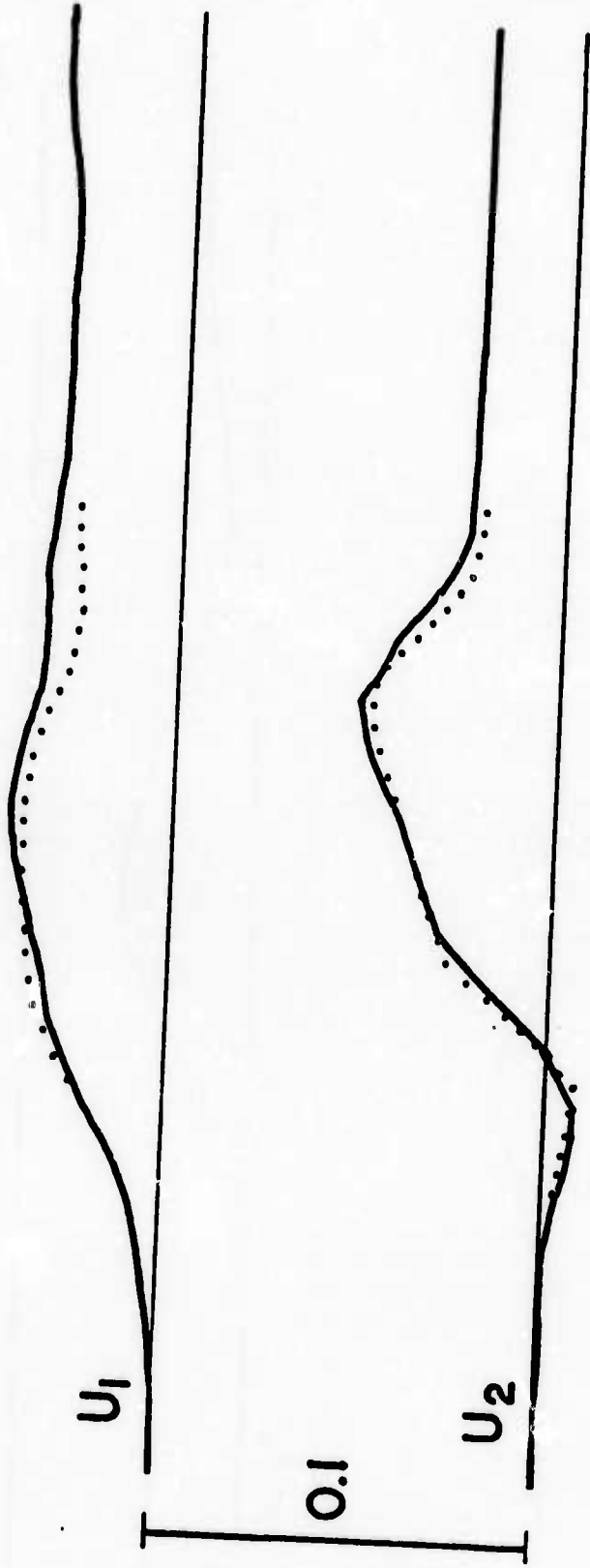
44

10



$v$

$\equiv$



46

